

pubs.acs.org/JPCL Letter

Mercury Chalcogenide Nanoplatelet—Quantum Dot Heterostructures as a New Class of Continuously Tunable Bright Shortwave Infrared Emitters

Stephanie M. Tenney, Victoria Vilchez, Mikayla L. Sonnleitner, Chengye Huang, Hannah C. Friedman, Ashley J. Shin, Timothy L. Atallah, Arundhati P. Deshmukh, Sandrine Ithurria, and Justin R. Caram*



Cite This: J. Phys. Chem. Lett. 2020, 11, 3473-3480



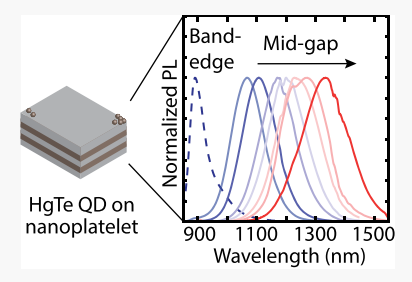
ACCESS

Metrics & More

Article Recommendations

3 Supporting Information

ABSTRACT: Despite broad applications in imaging, energy conversion, and tele-communications, few nanoscale moieties emit light efficiently in the shortwave infrared (SWIR, 1000-2000 nm or 1.24-0.62 eV). We report quantum-confined mercury chalcogenide (HgX, where X = Se or Te) nanoplatelets (NPLs) can be induced to emit bright (QY > 30%) and tunable (900–1500+ nm) infrared emission from attached quantum dot (QD) "defect" states. We demonstrate near unity energy transfer from NPL to these QDs, which completely quench NPL emission and emit with a high QY through the SWIR. This QD defect emission is kinetically tunable, enabling controlled midgap emission from NPLs. Spectrally resolved photoluminescence demonstrates energy-dependent lifetimes, with radiative rates 10-20 times faster than those of their PbX analogues in the same spectral



window. Coupled with their high quantum yield, midgap emission HgX dots on HgX NPLs provide a potential platform for novel optoelectronics in the SWIR.

Photons in the shortwave infrared (SWIR) spectral window are lower in energy than most molecular HOMO–LUMO gaps yet higher in energy than vibrational states. Without natural sources of background radiation or absorption, imaging in this spectral window shows superlative contrast and feature resolution. Decreased Rayleigh scatter for longer wavelength light also results in improved penetrative imaging through fog, foliage, skin, and bone. Fluorescence microscopy in the SWIR has already shown extraordinary background-free deep tissue imaging in living animals. Increasing the scope of SWIR absorbing and fluorescing materials may enable applications in sensing biological, chemical, or physical changes in complex and opaque environments.

Mercury chalcogenides make up a class of binary semi-conductors with narrow or negative band gaps used primarily in infrared photodetection. Like their more commonly studied cadmium chalcogenide analogs, quantum confined HgX (X = S, Se, Te) nanocrystals (NCs) can be synthesized with size-tuned band gaps that vary from near zero to 1 eV. Despite a few reports of high infrared quantum yields (QYs), HgX nanocrystals have not been extensively explored as compact fluorophores for the short or midwave infrared, unlike their PbX analogues. In this work, we demonstrate that ligand-exchanged two- and three-monolayer (ML) HgX nanoplatelets show previously unreported highly tunable emission in the SWIR while maintaining size-confined nanoplatelet absorption features. These materials represent a new platform for SWIR optoelectronics.

Recently, highly confined three-ML HgX nanoplatelets (NPLs) have been synthesized through a cation exchange from three-ML CdX NPLs using a mercury salt precursor. NPLs are two-dimensional (2D) structures with quantum confinement along their integer atomic thicknesses, where the number of monolayers is defined by the number of anionic layers; e.g., a three-ML HgX NPL will consist of three layers of X and four layers of Hg. The spatial extent, material constituents, and self-assembly of NPLs can be tuned to achieve an extremely versatile set of photophysical properties and applications, including a near unity exciton and biexciton quantum yield, efficient lasing, electroluminescence, and use as substrates for photodetectors.

Building upon previous work, we find that ligand exchange of two and three monolayer HgSe and HgTe NPLs produces growth of emissive QD-like defects on the NPL surface, similar to dot-on-platelet heterostructures. This gives a continuously tunable set of midgap states with a high degree of synthetic control over the wavelength of emission arising from the colloidal growth of the QD while maintaining a high QY. In the exemplar case, three-ML HgTe exhibits tuned narrowband

Received: March 26, 2020 Accepted: April 15, 2020 Published: April 15, 2020





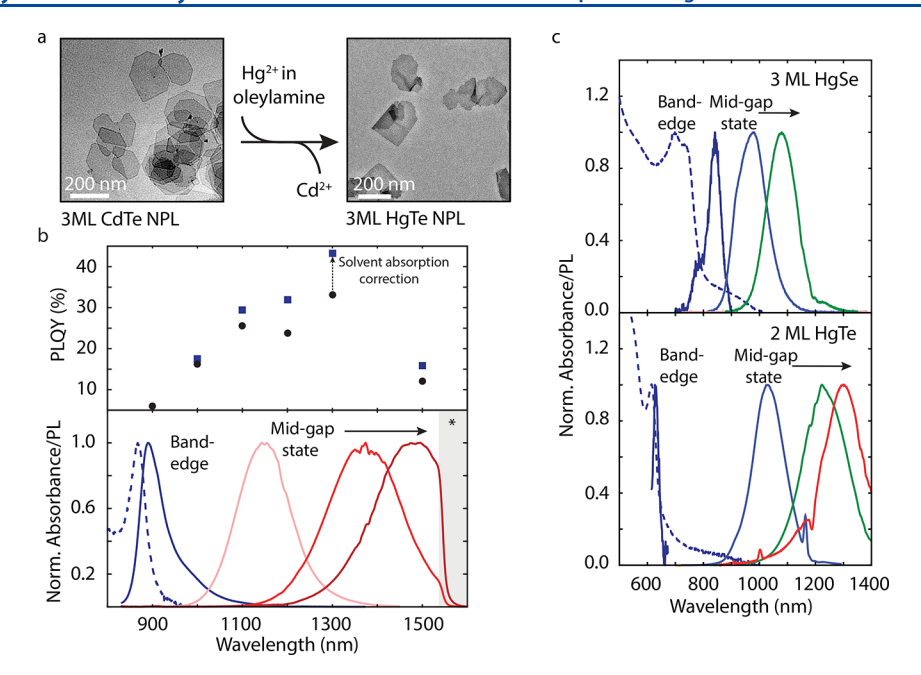


Figure 1. TEM shows the morphology of the NPLs is maintained after exchange. (b) Absorption (dashed line) and PL (solid lines) of three-ML HgTe NPL show band-edge emission after synthesis and midgap emission that appears and red-shifts over the following days. Typical QYs for these states are 25–35%. The PL spectra are corrected for solvent absorption to better visualize the position and width. Uncorrected data and details are provided in the Supporting Information. (c) Cation exchange in three-ML HgSe and two-ML HgTe shows similar behavior.

emission from 1000 to 1500 nm with a full width at halfmaximum (fwhm) of ~100-200 meV and a QY of >30% across this range. Although the emission line widths are slightly broader than those of highly monodisperse PbS QDs, these properties match those of the most emissive PbX/InAs quantum dots²⁴⁻²⁶ without any synthetic optimization, and the emission is stable over several months. We correlate the exchange of ligand type to the formation and tunability of the SWIR emission and demonstrate how kinetic conditions influence its rate of evolution. Finally, using superconducting nanowire single-photon detectors (SNSPDs), we obtain timeresolved band-edge and sub-band emission showing that the radiative lifetime is significantly faster than that of PbX analogues. Our results suggest that HgX NPLs are potential substrates for tunable fluorescent applications, including lighting, imaging, and materials for luminescent solar concentrators.

Synthesis of SWIR Emitting NPLs. We synthesize HgX NPLs based on the cation exchange procedures developed by Izquierdo et al. 14,28 (details provided in the Supporting Information). For example for three-ML HgTe NPLs, three-ML CdTe NPLs are first synthesized using slow injection of trioctylphosphine telluride into a degassed solution of the cadmium propionate precursor and oleic acid in octadecene at 215 °C.²⁹ Once the reaction is complete, the NPLs are purified by precipitation and resuspended in hexanes. FTIR spectroscopy of the CdTe NPLs shows that they are passivated with acetate and/or oleate ligands after synthesis (Figure S7). To exchange to HgTe, mercury (II) acetate is dissolved in oleylamine and introduced at room temperature to a solution of CdTe NPLs in hexanes [ranging from 2.4% to 16% (v/v)]. Ligand exchange accompanies cation exchange where acetate and oleate are exchanged for oleylamine (Figure S8), and transmission electron microscopy confirms that the morphology of the NPL is maintained (Figure 1a). A similar procedure

is used for the synthesis and exchange of CdSe with HgSe as described in the Supporting Information.

We monitor the progress of the cation exchange using absorbance and photoluminescence (PL) (Figure S9). Unlike previously reported NPL cation exchanges, when PL is monitored several hours after exchange a bright Stokes-shifted emission (~1000–1100 nm) appears along with band-edge emission (Figure 1b). This new emissive state shifts further into the infrared as a function of time while the band-edge emission is quenched. Despite large continual changes in observed emission, features in the absorption spectrum do not proportionally shift. The PL line width of the red-shifted emission is approximately 200–300 nm, and the quantum yield (QY) remains high, centered around 30% (Figure 1b) but reaching 56% in some preparations (Figure S6).

The high QY is consistent across a number of different samples and appears to be stable over an extended period of time. The absolute QY measured across different wavelengths gives values between 10% and 56% (Figure S6), and systematic error is explored using relative QY determination with a SWIR emitting dye standard giving a consistent value of 18% (Figure S7). These reported values do not account for losses due to solvent re-absorption; however, we apply a correction to our QY for the re-absorption of hexanes in Figure 1b (details in the Supporting Information). After the NPLs had been aged for 8 months, we see they retain a QY of 32% (Figure S6), which indicates the long-term stability of the emissive species. Furthermore, this behavior consistently occurs given the appropriate set of synthetic conditions and extends to other systems of HgX NPLs such as two-ML HgTe and three-ML HgSe, suggesting the mechanism of bright midgap state evolution may be general and applicable to other materials (Figure 1c).

Mechanistic Study of Midgap State Formation. We explored several mechanisms that could give rise to a large Stokesshifted emission. We discount the possibility of retaining any

Cd in the three-ML structure by energy dispersive X-ray (EDX) measurements that show complete exchange (Figure S10) as well as a loss of CdTe features in the absorption spectrum indicating no formation of type II CdTe/HgTe heterostructures²⁸ or Cd_xHg_{1-x}Te NPL alloys.³⁰ A lack of change in the NPL absorption spectrum suggests that neither aggregation nor relaxation of quantum confinement through the growth of thicker NPLs plays a role in the emission. We also do not observe any intraband transitions in the absorption spectrum that could be indicative of electronic doping due to the surface chemistry.³¹ Therefore, we hypothesize that a midgap state is induced by conditions used during exchange,³² especially as we do not observe midgap emission from the CdTe NPLs prior to the addition of Hg in OLA. Immediately after synthesis, we see no absorption features beyond the band edge of the NPL; however, in aged samples (5 months), we see features that resemble those of HgTe QDs. This suggests that the SWIR emission arises from room-temperature colloidal growth of HgX nanoparticles following cation exchange. 11,33,34 We assign the midgap emission to these QDs as the spectral changes follow the expected mechanisms of colloidal growth and energy transfer; however, we cannot definitively reach a conclusion about the mechanism of nucleation of QD or direct attachment onto the NPL. Our structural understanding arises from changes in the NPL, and further studies are needed to elucidate the nature of the QDs. Nonetheless, we find the formation of sub-band emission to be general in HgX NPLs with varying compositions and thicknesses and focus our efforts on the three-ML HgTe NPLs to explore the parameters that give rise to the observed emission.

To explore the role of the exchange parameters in the evolution of the midgap state, we vary (i) the amount of Hg added in excess to the amount of Cd in the CdTe NPL (Cd:Hg ratio), (ii) the amount of oleylamine added in conjunction with Hg2+ during exchange, and (iii) the length of time the colloidal system is left in a solution of hexanes after exchange. In Figure 2, we show how the PL changes for a matrix of these synthetic variables. In Figure 2a, we plot the band-edge emission obtained directly after cation exchange and the evolution of the midgap emission, monitored over 75 days [although the temperature can control the rate (Figure [S19]. The midgap emission red-shifts rapidly in the days immediately after exchange and slows over longer time scales toward a maximum that appears to be intrinsic to the amount of excess Hg added (Figure 2b). In general, we obtain further red-shifted emission with greater excesses of Hg, but having an excess is not strictly necessary to induce formation; we see evolution occur when using a 1:1 ratio (Cd:Hg). We also explore the influence of oleylamine (Figure 2c) by changing the concentration of dissolved Hg and monitoring the PL after exchange (shown after 5 days). We find that a larger excess of Hg will produce a larger red-shift while a larger excess of oleylamine suppresses the rate of this shift. Therefore, the final position of the midgap emission wavelength can be tuned through the control of precursors.

Our results suggest that the formation of an emissive subband state requires both cation and ligand exchange. During the cation exchange reaction, the NPLs also experience a change in coating from oleic acid/oleate ligand to oleylamine (confirmed using FTIR in Figure S8). The formation of midgap emission is thus accompanied by an exchange from X-type ligands $[Hg(O_2R)_2]$ with L-type ligands such as oleylamine (by the Green nomenclature). 35 X-Type ligands

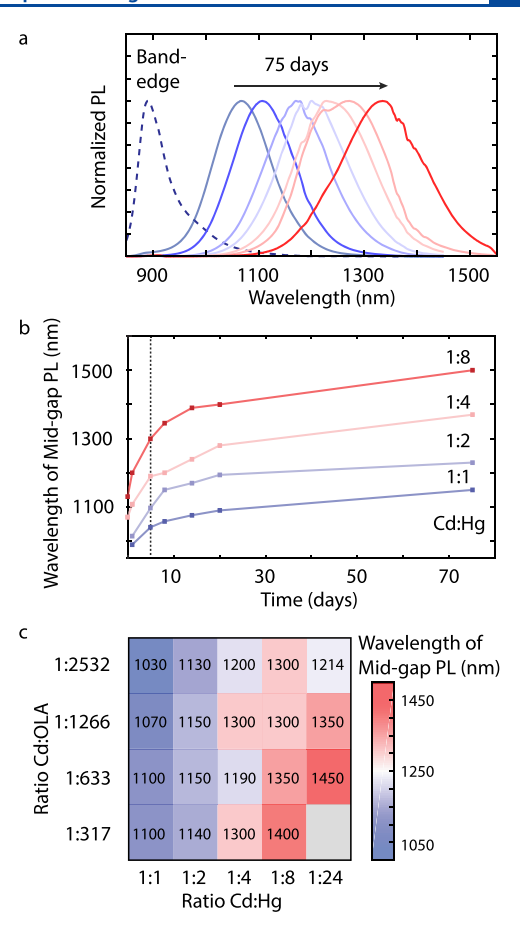


Figure 2. (a) Evolution of midgap emission over time for the 1:4:1266 Cd:Hg:OLA ratio used during exchange. The spectra have been corrected for solvent absorption as described in the Supporting Information. (b) The depth of the midgap state can be varied by changing the Cd:Hg ratio used during exchange. (c) Synthetic conditions explored to induce midgap emission by changing the concentration of Hg^{2+} in oleylamine (OLA), relative to that of cadmium. The wavelengths are reported for day 5 after synthesis (indicated by the dotted line in panel b).

are one-electron donors that form a covalent bond with the metal, while L-type ligands are two-electron donors (often a lone pair) that form a dative bond with the metal. This type of ligand exchange from X to L has been explored in CdSe NCs capped with oleic acid, where a displacement is observed when an L-type ligand is introduced into a carboxylate bound to a metal site. 32,36 Because the metal-carboxylate $[M(O_2R)_2]$ can act as a ligand itself, exchange with the L-type ligand removes a surface metal atom with two carboxylates as one unit. Similarly, in HgTe QDs, this type of ligand displacement can introduce intragap emission, which has been attributed to surface-localized states.³⁷ We hypothesize that following this mechanism, HgTe NPLs capped with oleic acid/oleate may undergo this type of exchange with oleylamine, removing some of the surface Hg atoms from the newly formed NPLs. This could then introduce surface sites or defects from undercoordinated Te or dangling bonds that are reactive toward the growth of QDs.

The absorption spectrum of the NPLs is also sensitive to ligand type, and we see a red-shift characteristic of an OA to OLA exchange. ^{14,36,38} In the case of exchange with a sterically hindered amine, such as triisobutylamine, we find that the NPLs do not experience this same behavior. They retain the

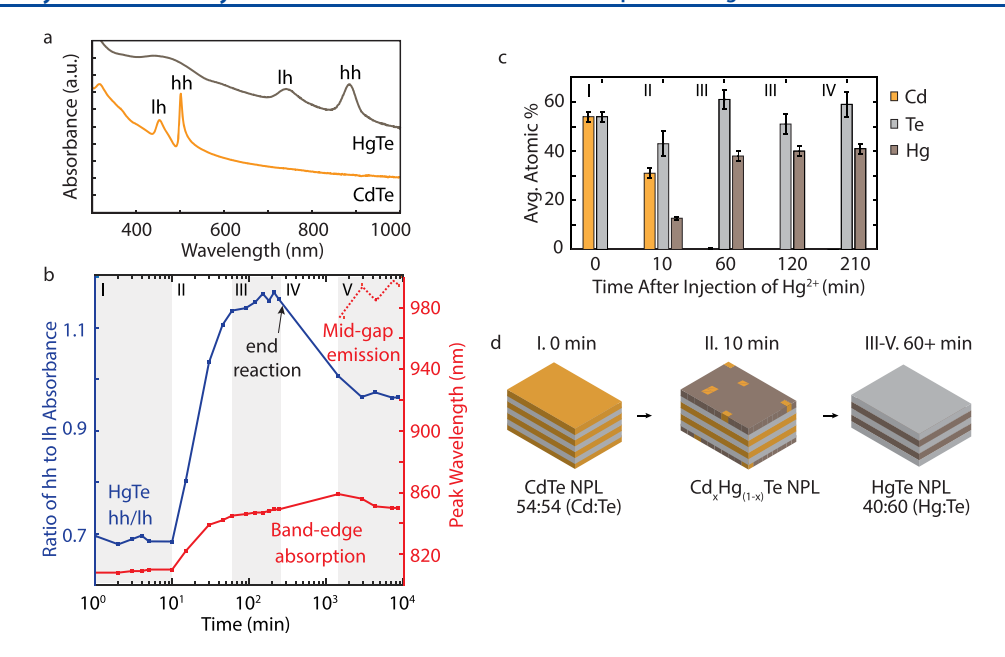


Figure 3. (a) Absorption spectra for CdTe and HgTe NPLs and their light hole (lh) and heavy hole (hh) features. (b) hh:lh HgTe ratio (blue line) and wavelength of hh (red line) monitored by changes in the absorption spectrum during different time points of exchange. The dashed line indicates the formation of midgap emission. (c) EDX monitoring stoichiometry changes during exchange. (d) Possible mechanism for observed stoichiometry changes where Hg atoms are removed from the NPL surfaces.

oleic acid/oleate and acetate ligands by FTIR (Figure S8), and while we do observe midgap emission, the evolution is arrested (Figure S15). In addition, the absorption and emission spectra do not show the slight red-shift as seen in the OA to OLA exchange. Ligand exchange does not appear to be occurring in the same manner, and midgap state evolution is hindered. This suggests that the interaction of oleylamine with the surface is critical for the evolution of QDs on the surface.

In Figure 3, we explore the emergence and evolution of the midgap emissive state through absorption, emission, and EDX spectroscopies. We find that the overall exchange is a multistep process that we qualitatively divide by significant changes in the absorption and photoluminescence spectra, beginning with cation exchange from CdTe to HgTe. The behavior is similar for different samples and conditions (Figure S16).

The rapid initial stage (I) occurs with the exchange of Cd with Hg. Removal of the Cd atoms happens within the first 10-15 min, as we see the CdTe hh/lh disappear and give rise to the HgTe hh/lh in the absorption spectrum (Figure 3a). These HgTe features then begin to red-shift and grow in intensity during the second stage (II). During this first hour, the formation of HgTe NPLs is monitored by the intensity of the hh/lh where the ratio is expected to be >1, indicating a complete exchange.¹⁴ We find that by the first hour, this ratio reaches 1.1 and EDX confirms the completed exchange of Cd with Hg (Figure 3c, 60 min). Moreover, the stoichiometry of the NPLs is 40:60 (Hg:Te), which suggests that Te is now in excess and supports the notion of loss of Hg atoms occurring simultaneously to a changing ligand environment. The 40:60 (Hg:Te) ratio suggests that surface Hg atoms are being stripped as Hg-oleate ligands are displaced by oleylamine, leaving two Hg layers and three Te layers in the NPL and changing the charge at the surface. This is surprising given the lack of a blue-shift in the absorption spectrum as would be expected by a stronger confinement in thinner NPLs. We cannot eliminate the possibility of severe depletion of Hg in the system (perhaps from internal Hg layers) while

maintaining the three-ML thickness, but further studies are needed to fully characterize the sites of Hg loss in the NPL.

From 1 to 4 h (III), the hh:lh ratio stabilizes around 1.1 while the wavelength of absorption gradually red-shifts toward 860–880 nm. During this stage, the Hg:Te ratio does not significantly change and Te remains in excess. Despite significant changes in stoichiometry during the total reaction (I–III), the loss of surface Hg atoms precedes midgap state emission and NPLs show only band-edge emission (~900 nm) by this time point.

In the hours following exchange (IV), there is a decrease in the hh:lh ratio suggesting some change in the electronic structure, potentially arising from the physical changes on the surface of the NPLs, although we see no continual changes in the stoichiometry (Table S1). After the NPLs had been washed at 3.5 h, the hh:lh ratio stabilizes again around 1. We mark the final stage (V) as the formation and evolution of midgap emission that occurs between 4 and 24 h after exchange, depending on the conditions explored in Figure 2. The band-edge absorption and emission remain around 880 and 900 nm, respectively, as the midgap emission begins to red-shift into the SWIR.

TEM of NPLs after exchange shows the presence of quantum dot-like moieties growing on or attached to NPLs in aged samples that show midgap emission (Figure 4a). These QDs survive washing steps by centrifugation and syringe filtering, suggesting that they are growing from the NPLs (possibly epitaxially) or attach to the NPLs after nucleation (Figure S13). Given the influence of the excess precursor in solution, this suggests that depletion of surface Hg atoms on the NPLs following ligand exchange with oleylamine may be giving rise to room-temperature colloidal growth of HgX nanoparticles that act as quantum-confined defects. The removal of surface atoms may be inducing a surface rearrangement or simply providing reactive sites for the growth of these nanoparticles without affecting the confinement of the NPLs, as seen in the absorption spectrum of aged

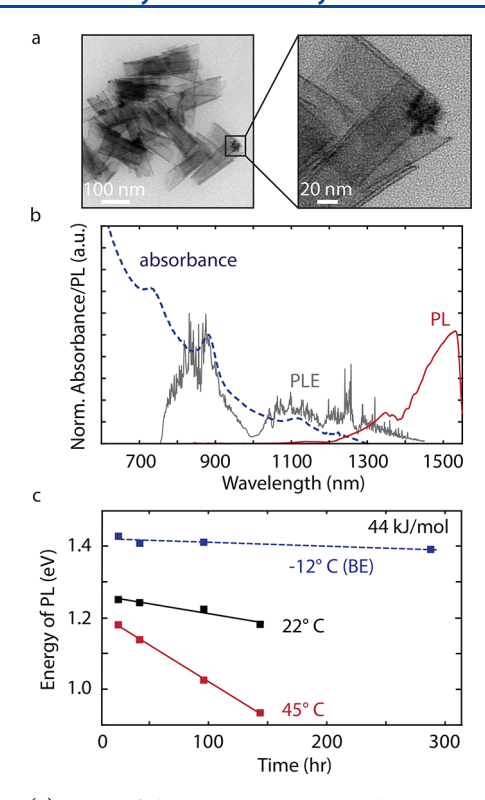


Figure 4. (a) TEM of three-ML HgTe NPLs showing quantum dot growth after aging. (b) Absorbance (blue dashed line), PL (red solid line), and PLE (gray solid line) for a sample aged for 5 months. (c) Energy of midgap PL from solutions held at elevated temperatures (solid lines) after exchange. When the samples are kept cold (blue dashed line), no shift from band-edge emission is observed.

samples showing only SWIR emission. Additionally, we see a dependence of temperature on the rate of evolution, which also suggests a growth mechanism. In Figure 4b, we monitor the evolution of the emission energy for the midgap state at three temperatures. We observe a significant rate of PL shift increase at elevated temperatures, which we fit to an activation barrier of 44 kJ/mol (Figure S20). These temperature kinetics are comparable to the bond energy in bulk HgTe (~78 kJ/mol)³⁹

and may be consistent with bond-forming or bond-breaking processes.

We hypothesize that the QDs are in direct contact with the NPLs due to the quenching of the NPL band-edge emission, suggesting a transfer of energy from a platelet to a dot, which is much faster than radiative recombination in the NPL. We believe that the system is experiencing a near field energy transfer rather than a FRET process where we would expect the QY to be limited to 10% by the donor (NPL band edge). Rather, we find that the QY is consistently higher than 10%, suggesting that the QD is either very close to or growing from the NPL surface.

Similar large Stokes-shifted emission due to defects has been seen in other colloidal NCs such as metal dopants in CuInSe₂ or CdSe/ZnS⁴⁰ and noncoordinated surface selenium in ultrasmall CdSe; ⁴¹ however, the tunability of these defect states is dependent on defect dopant concentration, and these systems do not display SWIR emission. Dot-on-nanoplatelet heterostructures have been observed for CdSe/ZnSe⁴² and more recently PbSe/CdSe, ⁴³ but these systems do not show the same continual room-temperature growth dynamics. Our mechanism produces a new type of heterostructure SWIR emitter with large Stokes shifts that can be tuned through the SWIR. Our data suggest that these emissive states may arise from energy transfer to defect-like SWIR-emitting nanoparticles attached to the NPLs that evolve over time, possibly through structural rearrangement or colloidal growth.

Comparison of Quantum Yields and Lifetimes. Using superconducting nanowire single-photon detectors and a time-tagged photon counting module, we are able to obtain time-resolved photoluminescence of SWIR-emitting NPLs at varying stages of midgap emission evolution (Figure 5a,b). NPLs showing only a band edge have an average lifetime of 7.4 ns, while those that show midgap emission from the QDs have an average lifetime of 130 ns (Table S2). Taking the QY of our SWIR-emitting QD on NPLs to be (0.3), this lifetime suggests a radiative rate of approximately 430 ns. Various midgap-emitting NPLs (regardless of their central wavelength) show similar dynamics (Figure S21), suggesting a common nature to the midgap emission regardless of depth. The carrier lifetimes for these SWIR-emitting HgTe NPLs are significantly shorter

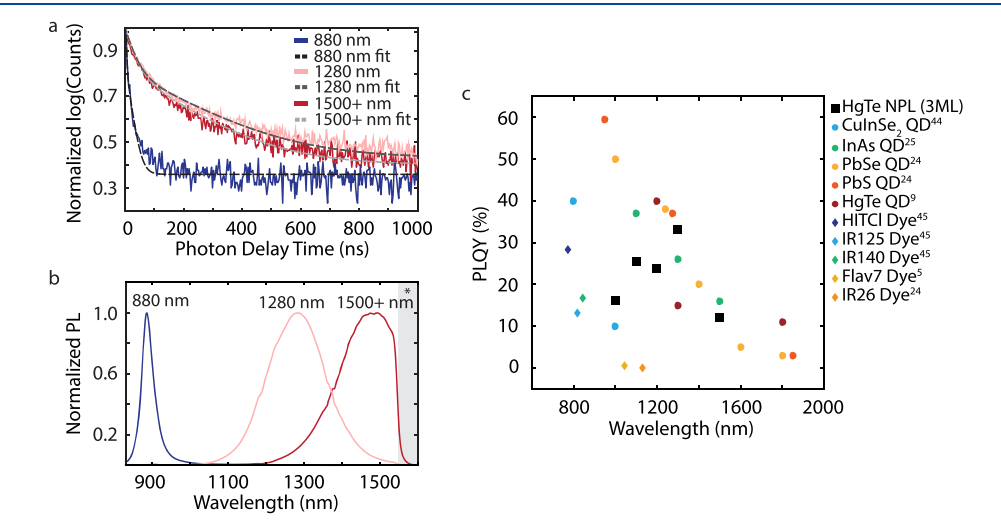


Figure 5. (a) Photoluminescence lifetimes from HgTe NPLs showing only the band edge (880 nm) and two samples with varying midgap emission (1280 and >1500 nm). (b) Corresponding PL spectra, which are corrected as described in the Supporting Information (Figure S21). The asterisk indicates the limit of the detector. (c) QYs of organic dye and QD fluorophores across the NIR/SWIR. 5,9,24,25,44,45

than those of PbS QDs, which are known to have lifetimes on the order of microseconds, ^{46–48} and slightly shorter than those of HgTe QDs, which are reported to be 480 ns. ³⁷ Recent work toward 2D PbS NPLs has shown great improvement toward decreasing these lifetimes, with values similar to those of this work (50–60 ns); however, tunability into the SWIR while maintaining a high QY has yet to be shown. ^{49–51} While maintaining fast radiative rates, our HgTe NPLs/QD heterostructures demonstrate high QYs that are competitive with other quantum dots that emit in this region of the spectrum (Figure 5c).

We show bright and continuously tunable midgap state emission in HgX NPL heterostructures by postsynthetic growth of QD-like surface defects. Quantum yields for these emissive states are >30%, making them comparable to those of the best infrared-emitting PbX and HgTe QDs, while showing markedly faster radiative rates of 430 ns without any added optimizations. We find that the energy of this midgap state is a function of both cation and ligand exchange properties and is consistent with slow activated growth of HgX QD defects on the NPL structure. The mechanism of SWIR evolution appears to be applicable to the family of HgX nanoplatelets, including two-ML HgTe and three-ML HgSe. Their highly tunable emission and radiative lifetimes while maintaining the large area NPL morphology give them potential applications in higher-flux light emission technologies, such as light-emitting diodes, sensors, and single-photon emitters.

ASSOCIATED CONTENT

Supporting Information

The Supporting Information is available free of charge at https://pubs.acs.org/doi/10.1021/acs.jpclett.0c00958.

Experimental details, including methods, additional optical characterization, and elemental and structural analysis (absorption and PL, EDX, FTIR, and TEM) (PDF)

AUTHOR INFORMATION

Corresponding Author

Justin R. Caram — Department of Chemistry and Biochemistry, University of California, Los Angeles, Los Angeles, California 90095-1569, United States; oocid.org/0000-0001-5126-3829; Email: jcaram@chem.ucla.edu

Authors

Stephanie M. Tenney – Department of Chemistry and Biochemistry, University of California, Los Angeles, Los Angeles, California 90095-1569, United States

Victoria Vilchez — Department of Chemistry and Biochemistry, University of California, Los Angeles, Los Angeles, California 90095-1569, United States

Mikayla L. Sonnleitner — Department of Chemistry and Biochemistry, University of California, Los Angeles, Los Angeles, California 90095-1569, United States

Chengye Huang — Department of Chemistry and Biochemistry, University of California, Los Angeles, Los Angeles, California 90095-1569, United States

Hannah C. Friedman – Department of Chemistry and Biochemistry, University of California, Los Angeles, Los Angeles, California 90095-1569, United States

- Ashley J. Shin Department of Chemistry and Biochemistry, University of California, Los Angeles, Los Angeles, California 90095-1569, United States
- Timothy L. Atallah Department of Chemistry and Biochemistry, University of California, Los Angeles, Los Angeles, California 90095-1569, United States
- Arundhati P. Deshmukh Department of Chemistry and Biochemistry, University of California, Los Angeles, Los Angeles, California 90095-1569, United States
- Sandrine Ithurria Laboratoire de Physique et d'Étude des Matériaux, PSL Research University, CNRS UMR 8213, ESPCI ParisTech, 75005 Paris, France; ⊚ orcid.org/0000-0002-4733-9883

Complete contact information is available at: https://pubs.acs.org/10.1021/acs.jpclett.0c00958

Author Contributions

S.M.T. and V.V. performed the synthesis and characterization with help from M.L.S. C.H. performed the kinetic experiments and calculations. A.J.S. determined photoluminescence lifetimes, and A.P.D. assisted with TEM imaging. T.L.A. and H.C.F. assisted with synthesis, photophysical characterization, and solvent re-absorption calculations.

Notes

The authors declare no competing financial interest.

ACKNOWLEDGMENTS

The authors thank Prof. Ellen Sletten, Prof. Miguel Garcia-Garibay, Prof. Yu Huang, Chuancheng Jia, and the Materials Characterization Laboratory at University of California, Los Angeles (UCLA), for instrumentation. The authors acknowledge the use of instruments at the Electron Imaging Center for NanoMachines, supported by the National Institutes of Health (1S10RR23057 to Z.H.Z.), and CNSI at UCLA. This work was supported by the U.S. Department of Energy, Office of Science, Basic Energy Sciences, under Award DE-SC0019245. Partial support was given by the National Science Foundation under Grant 1905242. J.R.C. acknowledges the Faculty Career Development Award from the UCLA office of Equity, Diversity and Inclusion.

REFERENCES

- (1) Hansen, M. P.; Malchow, D. S. Overview of SWIR Detectors, Cameras, and Applications. *Proc. SPIE* **2008**, *6939*, *69390I*.
- (2) Miron, A.; Bensrhair, A.; Fedriga, R. I.; Broggi, A. SWIR Images Evaluation for Pedestrian Detection in Clear Visibility Conditions. In *IEEE Conference on Intelligent Transportation Systems, Proceedings*; ITSC, 2013; pp 354–359. DOI: 10.1109/ITSC.2013.6728257
- (3) Hong, G.; Diao, S.; Chang, J.; Antaris, A. L.; Chen, C.; Zhang, B.; Zhao, S.; Atochin, D. N.; Huang, P. L.; Andreasson, K. I.; Kuo, C. J.; Dai, H. Through-Skull Fluorescence Imaging of the Brain in a New near-Infrared Window. *Nat. Photonics* **2014**, *8* (9), 723–730.
- (4) Wan, H.; Du, H.; Wang, F.; Dai, H. Molecular Imaging in the Second Near-Infrared Window. Adv. Funct. Mater. 2019, 29, 1900566.
- (5) Cosco, E. D.; Caram, J. R.; Bruns, O. T.; Franke, D.; Day, R. A.; Farr, E. P.; Bawendi, M. G.; Sletten, E. M. Flavylium Polymethine Fluorophores for Near- and Shortwave Infrared Imaging. *Angew. Chem., Int. Ed.* **2017**, *56* (42), 13126–13129.
- (6) Melchior, H.; Fisher, M. B.; Arams, F. R. Photodetectors for Optical Communication Systems. *Proc. IEEE* **1970**, *58* (10), 1466–1486
- (7) Jagtap, A.; Goubet, N.; Livache, C.; Chu, A.; Martinez, B.; Gréboval, C.; Qu, J.; Dandeu, E.; Becerra, L.; Witkowski, N.; Ithurria, S.; Mathevet, F.; Silly, M. G.; Dubertret, B.; Lhuillier, E. Short Wave

- Infrared Devices Based on HgTe Nanocrystals with Air Stable Performances. J. Phys. Chem. C 2018, 122, 14979.
- (8) Martinez, B.; Ramade, J.; Livache, C.; Goubet, N.; Chu, A.; Gréboval, C.; Qu, J.; Watkins, W. L.; Becerra, L.; Dandeu, E.; Fave, J. L.; Méthivier, C.; Lacaze, E.; Lhuillier, E. HgTe Nanocrystal Inks for Extended Short-Wave Infrared Detection. *Adv. Opt. Mater.* **2019**, 7 (15), 1900348.
- (9) Kovalenko, M. V.; Kaufmann, E.; Pachinger, D.; Roither, J.; Huber, M.; Stangl, J.; Hesser, G.; Schäffler, F.; Heiss, W. Colloidal HgTe Nanocrystals with Widely Tunable Narrow Band Gap Energies: From Telecommunications to Molecular Vibrations. *J. Am. Chem. Soc.* **2006**, *128* (11), 3516–3517.
- (10) Goubet, N.; Jagtap, A.; Livache, C.; Martinez, B.; Portalès, H.; Xu, X. Z.; Lobo, R. P. S. M.; Dubertret, B.; Lhuillier, E. Terahertz HgTe Nanocrystals: Beyond Confinement. *J. Am. Chem. Soc.* **2018**, 140 (15), 5033–5036.
- (11) Abdelazim, N. M.; Zhu, Q.; Xiong, Y.; Zhu, Y.; Chen, M.; Zhao, N.; Kershaw, S. V.; Rogach, A. L. Room Temperature Synthesis of HgTe Quantum Dots in an Aprotic Solvent Realizing High Photoluminescence Quantum Yields in the Infrared. *Chem. Mater.* **2017**, *29*, 7859.
- (12) Moreels, I.; Lambert, K.; Smeets, D.; De Muynck, D.; Nollet, T.; Martins, J. C.; Vanhaecke, F.; Vantomme, A.; Delerue, C.; Allan, G.; Hens, Z. Size-Dependent Optical Properties of Colloidal PbS Quantum Dots. ACS Nano 2009, 3 (10), 3023–3030.
- (13) Pietryga, J. M.; Schaller, R. D.; Werder, D.; Stewart, M. H.; Klimov, V. I.; Hollingsworth, J. A. Pushing the Band Gap Envelope: Mid-Infrared Emitting Colloidal PbSe Quantum Dots. *J. Am. Chem. Soc.* **2004**, *126* (38), 11752–11753.
- (14) Izquierdo, E.; Robin, A.; Keuleyan, S.; Lequeux, N.; Lhuillier, E.; Ithurria, S. Strongly Confined HgTe 2D Nanoplatelets as Narrow Near-Infrared Emitters. *J. Am. Chem. Soc.* **2016**, *138* (33), 10496–10501.
- (15) Tessier, M. D.; Mahler, B.; Nadal, B.; Heuclin, H.; Pedetti, S.; Dubertret, B. Spectroscopy of Colloidal Semiconductor Core/Shell Nanoplatelets with High Quantum Yield. *Nano Lett.* **2013**, *13* (7), 3321–3328.
- (16) Dufour, M.; Qu, J.; Greboval, C.; Méthivier, C.; Lhuillier, E.; Ithurria, S. Halide Ligands to Release Strain in Cadmium Chalcogenide Nanoplatelets and Achieve High Brightness. *ACS Nano* **2019**, *13* (5), 5326–5334.
- (17) Bertrand, G. H. V.; Polovitsyn, A.; Christodoulou, S.; Khan, A. H.; Moreels, I. Shape Control of Zincblende CdSe Nanoplatelets. *Chem. Commun.* **2016**, *52* (80), 11975–11978.
- (18) Naeem, A.; Masia, F.; Christodoulou, S.; Moreels, I.; Borri, P.; Langbein, W. Giant Exciton Oscillator Strength and Radiatively Limited Dephasing in Two-Dimensional Platelets. *Phys. Rev. B: Condens. Matter Mater. Phys.* **2015**, *91* (12), 121302 DOI: 10.1103/PhysRevB.91.121302.
- (19) Abécassis, B.; Tessier, M. D.; Davidson, P.; Dubertret, B. Self-Assembly of CdSe Nanoplatelets into Giant Micrometer-Scale Needles Emitting Polarized Light. *Nano Lett.* **2014**, *14* (2), 710–715.
- (20) Diroll, B. T.; Cho, W.; Coropceanu, I.; Harvey, S. M.; Brumberg, A.; Holtgrewe, N.; Crooker, S. A.; Wasielewski, M. R.; Prakapenka, V. B.; Talapin, D. V.; Schaller, R. D. Semiconductor Nanoplatelet Excimers. *Nano Lett.* **2018**, *18* (11), 6948–6953.
- (21) Nasilowski, M.; Mahler, B.; Lhuillier, E.; Ithurria, S.; Dubertret, B. Two-Dimensional Colloidal Nanocrystals. *Chem. Rev.* **2016**, *116* (18), 10934–10982.
- (22) She, C.; Fedin, I.; Dolzhnikov, D. S.; Dahlberg, P. D.; Engel, G. S.; Schaller, R. D.; Talapin, D. V. Red, Yellow, Green, and Blue Amplified Spontaneous Emission and Lasing Using Colloidal CdSe Nanoplatelets. *ACS Nano* **2015**, *9* (10), 9475–9485.
- (23) Chen, Z.; Nadal, B.; Mahler, B.; Aubin, H.; Dubertret, B. Quasi-2D Colloidal Semiconductor Nanoplatelets for Narrow Electroluminescence. *Adv. Funct. Mater.* **2014**, 24 (3), 295–302.
- (24) Semonin, O. E.; Johnson, J. C.; Luther, J. M.; Midgett, A. G.; Nozik, A. J.; Beard, M. C. Absolute Photoluminescence Quantum

- Yields of IR-26 Dye, PbS, and PbSe Quantum Dots. J. Phys. Chem. Lett. 2010, 1 (16), 2445-2450.
- (25) Franke, D.; Harris, D. K.; Chen, O.; Bruns, O. T.; Carr, J. A.; Wilson, M. W. B.; Bawendi, M. G. Continuous Injection Synthesis of Indium Arsenide Quantum Dots Emissive in the Short-Wavelength Infrared. *Nat. Commun.* **2016**, 7, 12749 DOI: 10.1038/ncomms12749.
- (26) Weidman, M. C.; Beck, M. E.; Hoffman, R. S.; Prins, F.; Tisdale, W. A. Monodisperse, Air-Stable PbS Nanocrystals via Precursor Stoichiometry Control. *ACS Nano* **2014**, 8 (6), 6363–6371.
- (27) Meinardi, F.; Colombo, A.; Velizhanin, K. A.; Simonutti, R.; Lorenzon, M.; Beverina, L.; Viswanatha, R.; Klimov, V. I.; Brovelli, S. Large-Area Luminescent Solar Concentrators Based on 'Stokes-Shift-Engineered' Nanocrystals in a Mass-Polymerized PMMA Matrix. *Nat. Photonics* **2014**, *8* (5), 392–399.
- (28) Izquierdo, E.; Dufour, M.; Chu, A.; Livache, C.; Martinez, B.; Amelot, D.; Patriarche, G.; Lequeux, N.; Lhuillier, E.; Ithurria, S. Coupled HgSe Colloidal Quantum Wells through a Tunable Barrier: A Strategy to Uncouple Optical and Transport Band Gap. *Chem. Mater.* **2018**, *30* (12), 4065–4072.
- (29) Pedetti, S.; Nadal, B.; Lhuillier, E.; Mahler, B.; Bouet, C. C.; Abécassis, B. A.; Xu, X.; Dubertret, B. Optimized Synthesis of CdTe Nanoplatelets and Photoresponse of CdTe Nanoplatelets Films. *Chem. Mater.* **2013**, 25, 2455.
- (30) Gupta, S.; Zhovtiuk, O.; Vaneski, A.; Lin, Y. C.; Chou, W. C.; Kershaw, S. V.; Rogach, A. L. Cd x Hg (1-x) Te Alloy Colloidal Quantum Dots: Tuning Optical Properties from the Visible to near-Infrared by Ion Exchange. *Part. Part. Syst. Charact.* **2013**, 30 (4), 346–354.
- (31) Deng, Z.; Jeong, K. S.; Guyot-Sionnest, P. Colloidal Quantum Dots Intraband Photodetectors. *ACS Nano* **2014**, *8* (11), 11707–11714.
- (32) Singh, S.; Tomar, R.; Ten Brinck, S.; De Roo, J.; Geiregat, P.; Martins, J. C.; Infante, I.; Hens, Z. Colloidal CdSe Nanoplatelets, A Model for Surface Chemistry/Optoelectronic Property Relations in Semiconductor Nanocrystals. *J. Am. Chem. Soc.* **2018**, *140* (41), 13292–13300.
- (33) Mirzai, H.; Nordin, M. N.; Curry, R. J.; Bouillard, J. S.; Zayats, A. V.; Green, M. The Room Temperature Phosphine-Free Synthesis of near-Infrared Emitting HgSe Quantum Dots. *J. Mater. Chem. C* **2014**, 2 (12), 2107–2111.
- (34) Piepenbrock, M. O. M.; Stirner, T.; Kelly, S. M.; O'Neill, M. A Low-Temperature Synthesis for Organically Soluble HgTe Nanocrystals Exhibiting near-Infrared Photoluminescence and Quantum Confinement. J. Am. Chem. Soc. 2006, 128 (21), 7087–7090.
- (35) Green, M. L. H. A. New Approach to the Formal Classification of Covalent Compounds of the Elements. *J. Organomet. Chem.* **1995**, 500 (1–2), 127–148.
- (36) Anderson, N. C.; Hendricks, M. P.; Choi, J. J.; Owen, J. S. Ligand Exchange and the Stoichiometry of Metal Chalcogenide Nanocrystals: Spectroscopic Observation of Facile Metal-Carboxylate Displacement and Binding Scheme 1. Nanocrystal Ligand Binding Motifs According to the Covalent Bond Classification Method. *J. Am. Chem. Soc.* 2013, 135, 18536.
- (37) Geiregat, P.; Houtepen, A. J.; Sagar, L. K.; Infante, I.; Zapata, F.; Grigel, V.; Allan, G.; Delerue, C.; Van Thourhout, D.; Hens, Z. Continuous-Wave Infrared Optical Gain and Amplified Spontaneous Emission at Ultralow Threshold by Colloidal HgTe Quantum Dots. *Nat. Mater.* **2018**, *17* (1), 35–41.
- (38) Chen, O.; Yang, Y.; Wang, T.; Wu, H.; Niu, C.; Yang, J.; Cao, Y. C. Surface-Functionalization-Dependent Optical Properties of II-VI Semiconductor Nanocrystals. *J. Am. Chem. Soc.* **2011**, *133* (43), 17504–17512.
- (39) Chen, A.-B.; Sher, A. Semiconductor Alloys: Physics and Materials Engineering; Springer US, 1996.
- (40) Wu, K.; Li, H.; Klimov, V. I. Tandem Luminescent Solar Concentrators Based on Engineered Quantum Dots. *Nat. Photonics* **2018**, *12* (2), 105–110.

- (41) Bowers, M. J.; McBride, J. R.; Rosenthal, S. J. White-Light Emission from Magic-Sized Cadmium Selenide Nanocrystals. *J. Am. Chem. Soc.* **2005**, *127* (44), 15378–15379.
- (42) Yadav, S.; Adhikary, B.; Tripathy, P.; Sapra, S. Efficient Charge Extraction from CdSe/ZnSe Dots-on-Plates Nanoheterostructures. *ACS Omega* **2017**, *2* (5), 2231–2237.
- (43) Williams, K. R.; Diroll, B. T.; Watkins, N. E.; Rui, X.; Brumberg, A.; Klie, R. F.; Schaller, R. D. Synthesis of Type i PbSe/CdSe Dot-on-Plate Heterostructures with Near-Infrared Emission. *J. Am. Chem. Soc.* **2019**, *141* (13), 5092–5096.
- (44) Cassette, E.; Pons, T.; Bouet, C.; Helle, M.; Bezdetnaya, L.; Marchal, F.; Dubertret, B. Synthesis and Characterization of Near-Infrared Cu-In-Se/ZnS Core/Shell Quantum Dots for in Vivo Imaging. *Chem. Mater.* **2010**, 22 (22), 6117–6124.
- (45) Rurack, K.; Spieles, M. Fluorescence Quantum Yields of a Series of Red and Near-Infrared Dyes Emitting at 600–1000 Nm. *Anal. Chem.* **2011**, 83 (4), 1232–1242.
- (46) Clark, S. W.; Harbold, J. M.; Wise, F. W. Resonant Energy Transfer in PbS Quantum Dots. J. Phys. Chem. C 2007, 111 (20), 7302–7305.
- (47) Nienhaus, L.; Wu, M.; Geva, N.; Shepherd, J. J.; Wilson, M. W. B.; Bulović, V.; Van Voorhis, T.; Baldo, M. A.; Bawendi, M. G. Speed Limit for Triplet-Exciton Transfer in Solid-State PbS Nanocrystal-Sensitized Photon Upconversion. *ACS Nano* **2017**, *11* (8), 7848–7857.
- (48) Atallah, T. L.; Sica, A. V.; Shin, A. J.; Friedman, H. C.; Kahrobai, Y. K.; Caram, J. R. Decay-Associated Fourier Spectroscopy: Visible to Shortwave Infrared Time-Resolved Photoluminescence Spectra. *J. Phys. Chem. A* **2019**, *123* (31), 6792–6798.
- (49) Khan, A. H.; Brescia, R.; Polovitsyn, A.; Angeloni, I.; Martín-García, B.; Moreels, I. Near-Infrared Emitting Colloidal PbS Nanoplatelets: Lateral Size Control and Optical Spectroscopy. *Chem. Mater.* **2017**, 29 (7), 2883–2889.
- (50) Khan, S.; Jiang, Z.; Premathilka, S. M.; Antu, A.; Hu, J.; Voevodin, A. A.; Roland, P. J.; Ellingson, R. J.; Sun, L. Few-Atom-Thick Colloidal PbS/CdS Core/Shell Nanosheets. *Chem. Mater.* **2016**, 28 (15), 5342–5346.
- (51) Antu, A. D.; Jiang, Z.; Premathilka, S. M.; Tang, Y.; Hu, J.; Roy, A.; Sun, L. Bright Colloidal PbS Nanoribbons. *Chem. Mater.* **2018**, *30* (11), 3697–3703.